Thermohydrodynamic Analysis of Bump Type Gas Foil Bearings: A Model Anchored to Test Data

Luis San Andrés
Mast-Childs Professor
Fellow ASME
Turbomachinery Laboratory,
Texas A&M University,
College Station, TX 77843-3123
e-mail: lsanandres@tamu.edu

Tae Ho Kim
Senior Research Scientist
Energy Mechanics Research Center,
Korea Institute of Science and Technology,
39-1 Hawolgok-dong, Songbuk-gu,
Seoul, Korea 136-791
e-mail: thk@kist.re.kr

The paper introduces a thermohydrodynamic (THD) model for prediction of gas foil bearing (GFB) performance. The model includes thermal energy transport in the gas film region and with cooling gas streams, inner or outer, as in typical rotor-GFBs systems. The analysis also accounts for material property changes and the bearing components' expansion due to temperature increases and shaft centrifugal growth due to rotational speed. Gas inlet feed characteristics are thoroughly discussed in bearings whose top foil must detach, i.e., not allowing for subambient pressure. Thermal growths determine the actual bearing clearance needed for accurate prediction of GFB forced performance, static and dynamic. Model predictions are benchmarked against published measurements of (metal) temperatures in a GFB operating without a forced cooling gas flow. The tested foil bearing is proprietary; hence, its geometry and material properties are largely unknown. Predictions are obtained for an assumed bearing configuration, with bump-foil geometry and materials taken from prior art and best known practices. The predicted film peak temperature occurs just downstream of the maximum gas pressure. The film temperature is higher at the bearing middle plane than at the foil edges, as the test results also show. The journal speed, rather than the applied static load, influences more the increase in film temperature and with a larger thermal gradient toward the bearing sides. In addition, as in the tests conducted at a constant rotor speed and even for the lowest static load, the gas film temperature increases rapidly due to the absence of a forced cooling air that could carry away the recirculation gas flow and thermal energy drawn by the spinning rotor; predictions are in good agreement with the test data. A comparison of predicted static load parameters to those obtained from an isothermal condition shows the THD model producing a smaller journal eccentricity (larger minimum film thickness) and larger drag torque. An increase in gas temperature is tantamount to an increase in gas viscosity, hence, the noted effect in the foil bearing forced performance.
[DOI: 10.1115/1.3159386]

Keywords: gas foil bearing (GFB), thermal energy transport, thermohydrodynamics (THD), gas film temperature, static load parameters, rotordynamic force coefficients

1 Introduction

The widespread deployment of oil-free turbomachinery supported on gas foil bearings (GFBs) relies on overcoming intermittent contact and damaging wear at rotor start up and shut down, temporary rubs during normal operating conditions, and, most importantly, with engineered thermal management to ensure GFB performance in high-temperature environments [1]. Although gains have been made in specific loading [2,3], high-temperature material limits, coating endurance and stability, and adequate thermal management still restrict application of GFBs to high power density gas turbines [4].

The engineering of thermal energy transport in GFBs, or thermal management, as is customarily known in industry, is still eminently empirical and costly [5–7]. Poor thermal management due to inefficient cooling techniques and/or inadequate coatings can lead to catastrophic failure of the entire rotor-bearing system [6]. Incidentally, operation at high temperatures also determines significant changes in the static load and structural force coefficients of foil bearings [8–10]. For example, at a low frequency excitation of just 20 Hz, the bearing direct stiffness decreases by 50% when the shaft temperature increases from 22°C to 188°C [10].

The archival literature shows a few references that include modeling of heat flow transport in gas bearings. Salehi et al. [11] employed a *Couette* flow approximation to estimate the temperature field evolving around the bearing circumference. Comparison of exit temperature predictions to measurements in a generation I GFB are in reasonable agreement. Most important, however, is the finding that about 80% of the thermal energy is conducted by the top foil and advected to a cooling gas stream forced axially through one end of the bearing. The test bearing configuration may not be practical or efficient in an actual gas turbine engine.

Peng and Khonsari [12] introduced a conventional thermohydrodynamic (THD) model to predict the steady state performance of GFBs. A simple elastic foundation representing the bump-foil structure coupled to the Reynolds and thermal energy transport equations is solved simultaneously for prediction of the gas film pressure and temperature fields. In the model, a cooling gas stream flowing underneath the top foil largely determines the thermal characteristics of the bearing. Predictions reveal a nearly uniform film temperature along the bearing axial direction and an increase in load capacity, since gas viscosity typically increases with temperature. The authors note the excellent agreement of predicted temperatures to test data in Ref. [11], alas, the GFB model takes an arbitrary clearance to reproduce the measured tem-

Contributed by the International Gas Turbine Institute of ASME for publication in the JOURNAL OF ENGINEERING FOR GAS TURBINES AND POWER. Manuscript received March 24, 2009; final manuscript received March 30, 2009; published online January 26, 2010. Review conducted by Dilip R. Ballal. Paper presented at the ASME Gas Turbine Technical Congress and Exposition, Orlando, FL, June 8–12, 2009.

peratures. Incidentally, Ref. [12] implements an unrealistic gas feed model that allows for subambient gas pressures, not permitting top foil detachment.[1]

Le Lez [13] implemented a bulk-flow model to predict the gas film pressure and temperature fields in GFBs. The top foil and the bump strip layer are modeled as a nonlinear elastic foundation with dry friction between the bumps and the top foil and the bearing cartridge. The model uses an upwind scheme to solve the energy transport equation, which accounts for heat convection/conduction to the shaft and bearing housing. The THD model predicts a larger load capacity than an isothermal flow model with the same operating conditions; and where the gas film peak temperature increases as the journal eccentricity (load) increases. Reference [14] does not offer comparisons of predictions to test data.

Feng and Kaneko [14] presented finite element (FE) models of the Reynolds and energy transport equations predicting gas film pressure and temperature fields in multiple wound foil bearings. As in Ref. [12], the THD model predicts larger load capacity and drag torque than under isothermal (isoviscous) conditions. A comparison of model predictions to test data in Ref. [6] shows reasonable agreement, in spite of the arbitrary clearance used in the model and the physically implausible feed gas model introduced in Ref. [12].

In opposition to the THD predictions in Refs. [11–13], Della-Corte [15] reported a reduction in ~30% in load capacity for a test GFB when its operating temperature increases from 25°C to 650°C. Hence, as evidenced by test data in Refs. [8–10], temperature dependent mechanical properties of the structural components, thermal growth of the shaft and bearing, and shaft centrifugal growth need be accounted for the estimation of the operating clearance to obtain reliable predictions. Incidentally, bump-temperature data in Ref. [6] reveal a significant axial temperature gradient. The models in Refs. [11–13] neglect altogether this effect.

For flexure pivot tilting pad gas bearings, Sim and Kim [16] presented a THD model accounting for shaft thermal expansion and centrifugal growth. Predictions show that the gas film temperature increases as the rotor speed increases. The film temperature, nearly independent of the number of pads, hardly changes with increasing static loads. The model predicts larger direct stiffness and damping coefficients than an isothermal flow model, in particular, at high rotor speeds due to an increase in the gas viscosity and a decrease in the bearing actual clearance.

Thermal seizure and failure of a GFB are the result of inadequate thermal management and poor design with little consideration to the whole rotor-bearing system—thermal and structural. A microgas turbine manufacturer [17] notes that large gas film temperatures do not affect its proprietary GFB technology, since engineered thermal energy conduction paths in the bearing cartridge make for an adequate thermal management that has enabled the commercial success of its product application. Hence, the implementation of a realistic thermal model for GFBs must include not only the mechanical energy dissipation occurring within the gas film, but most importantly the heat convection and conduction paths into and out of the bounding surfaces (shaft and bearing) with due attention to the structural-thermal coupling that changes the GFB structural properties and components sizes, in particular shaft diameter and operating *minimum film* thickness.

2 THD and Thermal Lumped Parameters Model

Figure 1 shows a schematic view of a bump-type foil bearing supporting a rotating hollow journal. The graph depicts the coordinate systems and major components of the GFB. Figure 2 illustrates a side cut view of the bearing with two cooling gas streams, inner and outer. In practice, some bearings may include the outer (axial) gas stream only, while other bearings incorporate an inner gas stream through a hollow rotor [4,11]. In some applications, both gas streams may be needed. The depictions shown are representative only, not distinctive of actual configurations. For purposes of discussion only, consider—as in a gas turbine engine—the shaft is at a high temperature $T_{S(r)}$.

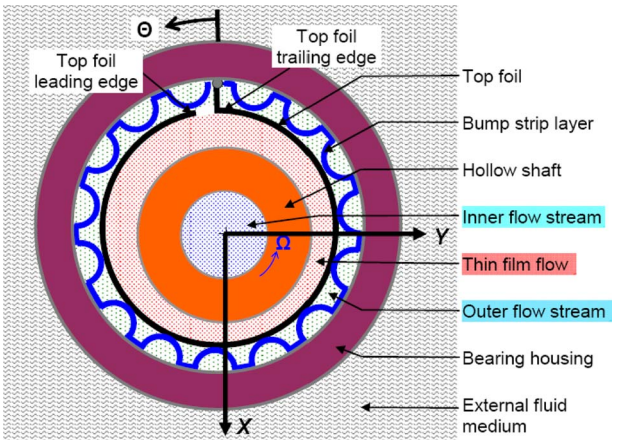

Fig. 1 Schematic view of gas foil bearing, components, and coordinate system

There is forced gas flowing axially through the thin film separating the rotor from the top foil front face. In this region, with minute film thickness (h_f), the gas hydrodynamic pressure (P_f) evolves while its temperature (T_f) varies. Here, mechanical power generated by fluid drag and heat convected from the *hot* rotor are removed by the gas film axial flow and also conducted into the top foil at temperature T_{F_i}. The outer flow stream, at upstream temperature and pressure (T_{C_o}, P_{C_o}), advects part of the heat from the back face of the top foil at temperature T_{F_o}. Heat also flows radially by conduction into the bearing cartridge at temperature, $T_{B(r)}$, and is disposed into the surroundings at temperature T_∞.

The outer flow, underneath the top foil, has a larger gap with characteristic length equal to a bump-foil height (Δ_B). Along ($0 \le z \le L$) the outer pressure decreases toward ambient (P_a) at $z = L$. The inner flow stream, at temperature and pressure (T_{C_i}, P_{C_i}),

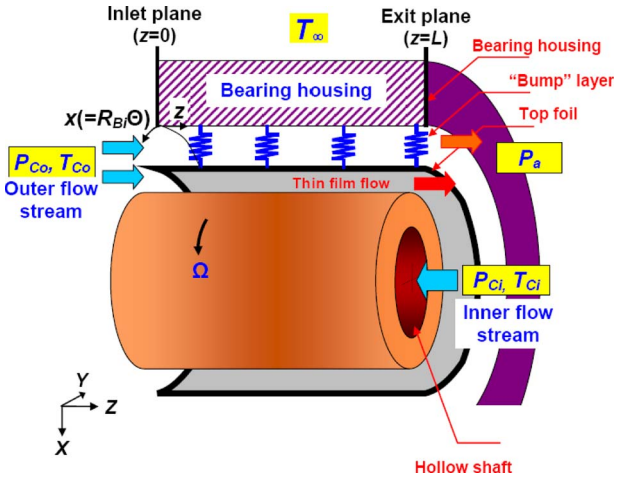

Fig. 2 Side view of bearing with inner cooling stream (T_{Ci}, P_{Ci}) flowing through hollow shaft and outer cooling stream (T_{Co}, P_{Co}) flowing through thin film region and underneath top foil. Outer cooling flow exits to ambient pressure (P_a).

[1]Note that a top foil underspring structure or bumps strip layer works only under compression, i.e., when the pressure on its top side is larger than that underneath. Otherwise, the bumps would either work under extension or would detach, both implausible physical conditions. Hence, the necessary condition of foil detachment to avoid a physically unrealistic subambient pressure to evolve.

cools the shaft inner surface at temperature T_{S_i}. The two cooling streams, inner and outer, are of sufficient strength to maintain their respective temperatures.

2.1 Hydrodynamic Pressure Generation and Temperature Transport in Thin Film Flow Region. The THD model for a GFB couples the Reynolds equation to the energy transport equation, accounting for a multilayer conduction/convection from the thin film into the bearing and into the shaft. Consider an ideal gas with density $\rho_f=(P_f/\Re_g T_f)$ and viscosity $\mu_f(T)$. Within the film flow domain, $\{\Theta_l \le \Theta = x/R_{S_o} \le \Theta_t; 0 \le z \le L\}$, the gas film thickness h_f is very small compared with the shaft radius (R_{S_o}) and bearing length (L), and the gas kinematic viscosity $(\upsilon=\mu/\rho)$ is relatively large. Hence, the flow regime within the gas film region is typically laminar and not influenced by fluid inertia (the circumferential flow Reynolds number is small, i.e., $\mathrm{Re}_h^*=\Omega h_f^2/\upsilon<1$).

Reynolds equation describes best the generation of the hydrodynamic film pressure P_f [18]

$$\frac{\partial}{\partial x}\left(\frac{h_f^3\rho_f}{12\mu_f}\frac{\partial P_f}{\partial x}\right)+\frac{\partial}{\partial z}\left(\frac{h_f^3\rho_f}{12\mu_f}\frac{\partial P_f}{\partial z}\right)=U_{m(z)}\frac{\partial}{\partial x}(\rho_f h_f) \tag{1}$$

with

$$U_m(z)=\frac{\Omega R_{S_o}}{2}(1-e^{-\delta z}) \tag{2}$$

as the mean shear-driven circumferential fluid velocity

$$\delta=\frac{12\mu_f}{(\dot{m}_z h^2)_f} \quad \text{and} \quad \dot{m}_z=\frac{{c_+}^2}{24\mu_{C_o}\Re_g T_{C_o}}\frac{({P_{C_o}}^2-{P_a}^2)}{L} \tag{3}$$

as the axial mass flow rate due to the forced pressure gradient from the outer cooling flow [19,20]. For a perfectly aligned journal, the film thickness in a simple GFB is [21]

$$h_f=c_+ + e_X\cos(\Theta)+e_Y\sin(\Theta)+w_d(P_f,T_f) \tag{4}$$

where c_+, e_X, e_Y, and w_d are the operating radial clearance, journal center displacements (e_X,e_Y), and top foil elastic deflection calculated from the 2D FE top foil structural model [22], respectively.

As detailed in Ref. [23], integration across the film thickness of the steady state thermal energy transport equation gives the bulk-flow equation for transport of gas film temperature

$$c_{p_f}\left(\frac{\partial(\rho_f h_f U_f T_f)}{\partial x}+\frac{\partial(\rho_f h_f W_f T_f)}{\partial z}\right)+\frac{1}{R_{S_o}}(\dot{Q}_{f\to F}+\dot{Q}_{f\to S})$$
$$=h_f\left(U_f\frac{\partial P_f}{\partial x}+W_f\frac{\partial P_f}{\partial z}\right)+\frac{12\mu_f}{h_f}\left\{W_f^2+\frac{1}{3}U_m+(U_f-U_m)^2\right\} \tag{5}$$

Above, the advection of heat by the gas flow plus the convection of heat $(\dot{Q}_{f\to F}+\dot{Q}_{f\to S})$ into the bounding surfaces equals the compression (reversible) work plus the dissipated mechanical energy. The momentum transport equations give the circumferential U_f and axial W_f bulk-flow velocities

$$U_f=U_{m(z)}-\frac{h_f^2}{12\mu_f}\frac{\partial P_f}{\partial x}, \quad W_f=-\frac{h_f^2}{12\mu_f}\frac{\partial P_f}{\partial z} \tag{6}$$

The outer flow gas stream (P_{C_o},T_{C_o}) sets the inlet conditions into the thin gas film. Note that the gas pressure underneath the top foil (outer flow region) varies axially as [18]

$$P_o(z)=\left[{P_{C_o}}^2\left(1-\frac{z}{L}\right)+P_a^2\left(\frac{z}{L}\right)\right]^{0.5} \tag{7}$$

For simplicity, the axial distribution of the gas temperature in the outer flow region (underneath the top foil) is ignored, i.e., $T_o(z)=T_{C_o}$. The boundary conditions for the inner film gas pressure and temperature fields are as follows.[2]

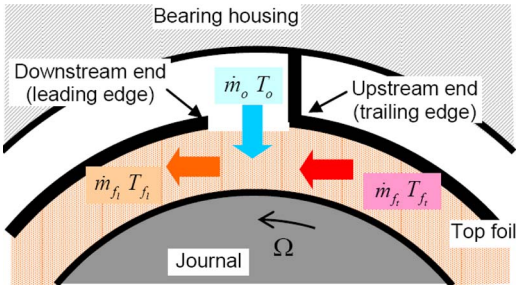

Fig. 3 Schematic view of thermal mixing conditions at gap between trailing edge and leading edge of top foil

At the inlet plane $z=0$,

$$\{\Theta_l \le \Theta \le \Theta_t\} \quad P_f(\Theta,0)=P_{C_o}, \quad T_f(\Theta,0)=T_{C_o} \tag{8}$$

At the leading and trailing edges of the top foil,

$$\{0 \le z \le L\} \quad P_f(\Theta_l,z)=P_f(\Theta_t,z)=P_o(z) \tag{9}$$

At the exit plane, $z=L$,

$$\{\Theta_l \le \Theta \le \Theta_t\} \quad P_f(\Theta,L)=P_a \tag{10}$$

Solution of Eq. (5) gives the gas exit temperature $T_f(\Theta,L)$ at $z=L$ and $T_{f_t}=T_f(\Theta_t,z)$ at the top foil trailing edge.

Top foil detachment prevents gas film pressures from falling below ambient, $P_f \ge P_a$ [21,24]. Hence, (fresh or cold) gas flowing from the axial sides of the bearing into the gas film is unlikely to occur. At the leading edge (Θ_l) of the top foil, flow and thermal energy mixing processes occur, as depicted in Fig. 3. A fraction λ of the upstream film flow $(\dot{m}_{f_t},T_{f_t})$ leaving the top foil at its trailing edge mixes with the cold gas stream $(\dot{m}_o,T_o)$. Simple mass conservation and energy balances give the leading edge mass flow $\dot{m}_{f_l}$ with temperature T_{f_l} as

$$\dot{m}_{f_l}=\lambda\dot{m}_{f_t}+\dot{m}_o \tag{11}$$

$$\dot{m}_{f_l}T_{f_l}=\lambda\dot{m}_{f_t}T_{f_t}+\dot{m}_o T_o \tag{12}$$

where $\dot{m}_{f_{l,t}}=\int_0^L(\rho_f h_f U_f)_{\Theta=\Theta_{l,t}}dz$. The thermal mixing parameter λ (<1) is empirical, a function of the bearing configuration and of the strength of the externally imposed cooling flow. Low values of λ ensure cool gas feed conditions, i.e., $T_{f_l}\sim T_o$. On the other hand, $\lambda\sim 1$ makes for a poor bearing design with little replenishment of fresh gas and too large temperature increases.

2.2 Lumped Parameter Thermal Model. The model integrates various radial heat flow paths, as given in Table 1, from the film toward the bearing outer surface and/or the outer cooling stream, and/or from the film into the inner cooling stream. Figure 4 provides definitions of all temperatures and radii for interfacial surfaces, as well as a simple representation of the multilayered heat conduction and convection.

For heat flowing from the gas film into an inner cooling stream,

$$\dot{Q}_{f\to S}=\dot{Q}_{\to S}=\dot{Q}_{S\to C_i}=\dot{Q}_{C_i}=R_{S_o}\{\bar{h}_{\mathrm{eq}_{\to S}}(T_f-T_{C_i})\} \tag{13}$$

[2]Reynolds equation for the pressure field is of elliptic type, requiring of boundary conditions on the entire closure of the flow domain. On the other hand, the temperature transport equation is of parabolic type with specified boundary conditions at the inlet plane(s) where the gas flow is supplied.

Table 1 Summary of radial heat flows (convection and conduction)

Heat flow per unit axial length	Description
	Heat flow toward the bearing outer surface
$\dot{Q}_{f\to F}=\dot{q}_{f\to F}R_{F_i}=\bar{h}_{fF}R_{F_i}(T_f-T_{F_i})$	Heat convected from thin film into top foil inner (front) surface
$\dot{Q}_{\to F}=\frac{\kappa_F}{\Delta_{t_F}}R_F(T_{F_i}-T_{F_o})$	Heat conducted through top foil (inner to outer surfaces)
$\dot{Q}_{F\to B}=\frac{\kappa_F}{\Delta_B}R_{B_{eq}}(T_{F_o}-T_{B_i})$	Heat conducted through bump foil—from top foil outer (back) surface into bearing inner surface
$\dot{Q}_{F\to C_o}=\bar{h}_{Fo}R_{F_o}(T_{F_o}-T_{C_o})$	Heat convected from the top foil back surface into cooling outer stream
$\dot{Q}_{B\to C_o}=\bar{h}_{Bo}R_{B_i}(T_{B_i}-T_{C_o})$	Heat convected from the bearing inner surface into cooling outer stream
$\dot{Q}_{\to B}=\frac{\kappa_B}{\ln(R_{B_o}/R_{B_i})}(T_{B_i}-T_{B_o})$	Heat conducted through bearing housing (inner to outer surface)
$\dot{Q}_{B\to\infty}=\bar{h}_{B\infty}R_{B_o}(T_{B_o}-T_\infty)$	Heat convected from bearing housing outer surface into ambient fluid medium
	Heat flow into the hollow shaft
$\dot{Q}_{f\to S}=\dot{q}_{f\to S}R_{S_o}=\bar{h}_{fS}R_{S_o}(T_f-T_{S_o})$	Heat convected from thin film into shaft outer surface
$\dot{Q}_{\to S}=\frac{\kappa_S}{\ln(R_{S_o}/R_{S_i})}(T_{S_o}-T_{S_i})$	Heat conducted through hollow shaft (outer to inner surfaces)
$\dot{Q}_{S\to C_i}=\bar{h}_{Si}R_{S_i}(T_{S_i}-T_{C_i})$	Heat from hollow shaft convected by cooling inner stream

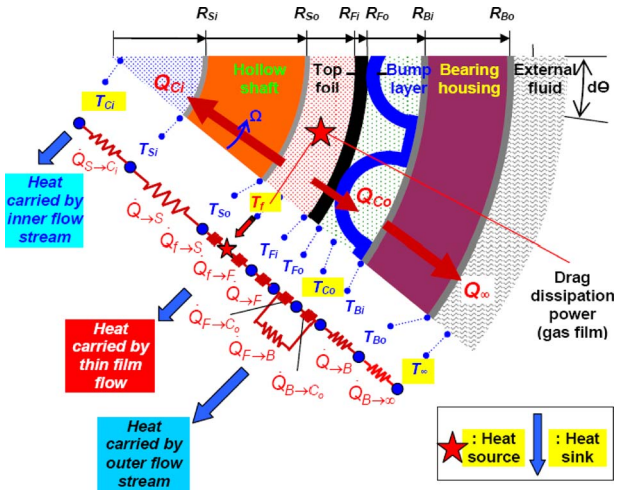

Fig. 4 Nomenclature for temperatures in GFB with cooling gas streams and schematic representation of heat flows

$$\frac{1}{\bar{h}_{\mathrm{eq}_{\to S}}}=\frac{1}{\bar{h}_{fS}}+\frac{R_{S_o}\ln\left(\frac{R_{S_i}}{R_{S_o}}\right)}{\kappa_S}+\frac{R_{S_o}}{\bar{h}_{Si}R_{S_i}} \tag{14}$$

film flow → hollow shaft → innercooling flow

where $\bar{h}_{\mathrm{eq}_{\to S}}$ is an equivalent heat transfer coefficient representing the heat convection from film into shaft, conduction through the shaft with outer and inner radii (R_{S_o},R_{S_i}) and material conductivity κ_S, and convection into the cooling stream.

For heat flowing into a (strong) outer cooling stream that carries away most of the heat from the back of the top foil and with little conduction into the bearing shell

$$\dot{Q}_{f\to F}=\dot{Q}_{\to F}=\dot{Q}_{F\to C_o}=\dot{Q}_{C_o}=R_{F_i}\{\bar{h}_{\mathrm{eq}_{\to o}}(T_f-T_{C_o})\} \tag{15}$$

$$\frac{1}{\bar{h}_{\mathrm{eq}_{\to o}}}=\frac{1}{\bar{h}_{fF}}+\frac{\Delta_{t_F}}{\kappa_F}+\frac{R_{F_i}}{R_{F_o}\bar{h}_{Fo}}$$

film flow → top foil → outer cooling flow (16)

where $\bar{h}_{\mathrm{eq}_{\to o}}$ is an equivalent heat convection coefficient, as also given in Ref. [12]. Above $R_{F_{i,o}}$ stands for the top foil inner and outer radii, and the metal foil has thickness Δ_{t_F} and thermal conductivity κ_F.

In the absence of an outer cooling stream, the heat transfer from the back of the top foil is by natural convection and conduction into the bearing through the bump strip layers

$$\dot{Q}_{f\to F}=\dot{Q}_{\to F}=\dot{Q}_{F\to B}+(\dot{Q}_{F\to C_o}+\dot{Q}_{B\to C_o})=\dot{Q}_{\to B}=\dot{Q}_{B\to\infty}$$
$$=R_{F_i}\{\bar{h}_{\mathrm{eq}_{\to B}}(T_f-T_\infty)\} \tag{17}$$

$$\frac{1}{\bar{h}_{\mathrm{eq}_{\to B}}}=\frac{1}{\bar{h}_{fF}}+\frac{1}{\frac{\kappa_F}{\Delta_{t_F}}}+\frac{1}{\left(\bar{h}_{Fo}+\bar{h}_{Bo}\frac{R_{B_i}}{R_{F_i}}\right)+\frac{1}{\frac{\Delta_B R_{F_i}}{\kappa_F R_{B_{eq}}}+\frac{R_{F_i}\ln\left(\frac{R_{B_o}}{R_{B_i}}\right)}{\kappa_B}+\frac{R_{F_i}}{\bar{h}_{B\infty}R_{B_o}}}} \tag{18}$$

film flow → top foil → bump strip layers → housing → ambient air
film flow → top foil → outer gap (between top foil and bearing housing inner surface)

where $\bar{h}_{\mathrm{eq}_{\to B}}$ represents a multilayer conduction/convection from the thin film into the bearing outermost surface exposed to ambient conditions. Above κ_B is the bearing material thermal conductivity, and $R_{B_{i,o}}$ are the bearing inner and outer radii. In addition, a bump equivalent radius $R_{B_{\mathrm{eq}}}=\Delta_{t_B}N_B/\pi$ denotes the narrow contact area (per axial length) of N_B bumps, each with thickness Δ_{t_B} and height Δ_B.

In Eqs. (14), (16), and (18) $\bar{h}_{fF}$ and $\bar{h}_{fS}$ are heat convection coefficients from the gas film into the top foil and shaft, respectively; $\bar{h}_{Fo}$ and $\bar{h}_{Bo}$ denote heat fluxes from the top foil back surface and the bearing housing inner surface, respectively, into the outer gap. Finally, $\bar{h}_{B\infty}$ represents the heat flux from the bearing outer surface (R_{B_o}) to its surroundings.[3] The heat convection coefficients are a function of the heat transfer characteristics, free or forced convection, and the flow condition, laminar or turbulent. Appendix A details formulas for the various heat convection coefficients in the THD model. Presently, for simplicity, heat through the bumps flows by conduction into the bearing cartridge with no disposal by convection into the outer gap flow.

For given input operating conditions, the limiting speed 1D-pressure field and journal eccentricity [25] serve to initiate the numerical solution of the steady state film flow equations (pressure and temperature). The solution procedure solves simultaneously the Reynolds equation (mass flow continuity) and thermal transport equations along a fixed axial coordinate. The forward marching procedure solves at a fixed axial location for the film pressure, and next for the film temperature, over the set of control volumes extending along the bearing circumference. Gas film properties, density, and viscosity are updated prior to marching downstream to the next set of control volumes. The procedure is iterative satisfying stringent constraints on the maximum differences in pressure and temperature fields. Note that the temperature field affects the operating bearing clearance due to shaft/bearing thermal growth, and also the foil support structural stiffness due to changes in the mechanical properties of the bearing cartridge and shaft and foil components. In the process, an outer iteration loop with a Newton–Raphson scheme updates the equilibrium journal position that generates the hydrodynamic gas pressure, creating a reaction force balancing the specified static load.

3 Model Validation: Predictions Versus Test Data in Ref. [6]

Radil and Zeszotek [6] presented measurements of temperature in a generation III GFB for a number of operating conditions, including changes in load and rotor speed, and at room temperature (21°C). The test GFB has an axial length $L=41$ mm and a diameter $D=50$ mm. Note however that Ref. [6] does not detail[4] the foil material or the bump strip layers geometry and disposition. For an applied static load increasing from 9 N to 222 N, and after reaching steady state (15 min or more), thermocouples tack welded beneath certain bumps record metal temperatures. The measurements evidence a quick increase in temperature as soon as the rotor spins due to its tight assembly clearance. Note that the bearing dead weight is just 9 N. The recorded temperatures increase as both the rotor speed and static load increase. The peak temperature is measured along the bearing midplane and along the loading direction, and not at the bearing side edges where the film thickness is (presumed) minimal. Measurements also show significant axial temperature gradients as the rotor speed increases.

[3]Note to reader: thermal radiation conditions are not discussed for simplicity. They are accounted for, however.

[4]This deficiency is not unusual since foil bearing technology is guarded closely by its manufacturers. Most unusual is the ability of prior analyses to predict closely the measurements without knowledge of the bearing geometry and operating conditions. See Refs. [11,12,14], for example.

Table 2 Geometry and operating conditions of test GFB and hollow shaft

Parameters[a]	Value	Comment
Bearing cartridge and shaft		
Bearing inner radius, $R_{B_i}=D/2$	25 mm	Ref. [6]
Bearing length, L	41 mm	Ref. [6]
Bearing thickness, t_B	13 mm	Assumed
Shaft thickness, t_S	13 mm	Assumed
Nominal radial clearance, c	20 μm	Assumed
Top foil and bump strip layer		
Top foil thickness, Δ_{t_F}	127 μm	Ref. [7]
Bump-foil thickness, Δ_{t_B}	127 μm	Ref. [7]
Bump half length, l_B	1.778 mm	Ref. [26]
Bump pitch, s_0	4.064 mm	Ref. [26]
Bump height, Δ_B	0.580 mm	Ref. [26]
No. of bumps, $N_b\times$ strips, N_s	39×1	
Bump-foil Young's modulus, E	200 GPa	
Bump-foil Poisson's ratio, ν	0.31	
Bump-foil stiffness, k_B [b]	10.4 GN/m^3	
Air properties at 294.3 K (21°C) and ambient pressure, $P_a=1$ bar		
Gas Constant, $\Re_g$	287 J/kg K	
Density, ρ	1.164 kg/m^3	
Viscosity, μ	$(4\times10^{-8}T+5\times10^{-6})$ Pa s	
	1.82×10^{-5} Pa s at 294.3 K	
Conductivity, κ	$(7.0\times10^{-5}T+0.0042)$W/m K	
	0.0257 W/m K at 294.3 K	
Specific heat, c_p	$(0.0996T+1009.3)$ J/(kg K)	
	1020 J/(kg K) at 294.3 K	

[a]Reference [27] details material properties for air. Reference [28] details material properties for Inconel 718 bearing cartridge and shaft and Inconel X750 top foil and bump strip layer.

[b]Calculated using Iordanoff's formulas in Ref. [29].

Table 2 details the dimensions and materials for the bearing cartridge, top foil and bump strip layer, and gas operating conditions. The table notes either a source or an assumption-based on experience-for each parameter listed. Reference [6] does not give complete information on the materials and geometry of the test bearing, cartridge, and rotor. There is scant information on the operating conditions and thermal state of the rotor, for example. Note that the actual operating clearance is determined from thermal changes in the material properties and the components' thermal and centrifugal growths.

Although the lumped parameter thermal model integrates various heat flow paths due to a forced cooling flow and inner and outer with temperatures (T_{ci},T_{co}) different from ambient (T_a), the predictions are limited to a GFB operating without a cooling stream for comparison to test data in Ref. [6] and taking $T_{ci}=T_{co}=T_a$.

In operation, the bearing clearance is $c_+=c-S_C-S_T$, where S_T and S_C are the thermal expansion and centrifugal growth due to rotor spinning, respectively. For a hollow shaft

$$S_T\approx\alpha_T(R_{S_o}-R_{S_i})(T_{S_m}-T_\infty) \tag{19}$$

where α_T is the shaft material thermal expansion coefficient and T_{S_m} is an average shaft temperature. Note that the bearing material thermal expansion is calculated in the same manner.

The shaft centrifugal growth ($S_C\sim\Omega^2$) is a function of its geometry and material properties [30]

$$S_C=\frac{R_{S_o}\rho_S\Omega^2}{8E_S}\{(1-\nu_S)A_1+(1-\nu_S)A_2-(1-\nu_S^2)R_{S_o}^2\}$$

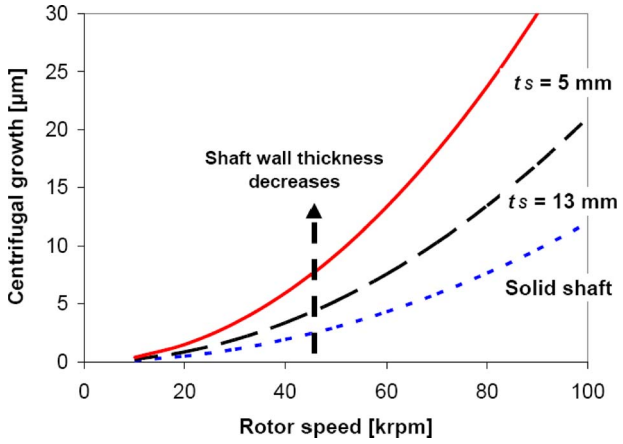

Fig. 5 Shaft centrifugal growth versus rotor speed. Solid shaft and hollow shafts (thin and thick wall thicknesses). Material Inconel 718. Shaft outer diameter of 50 mm and wall thickness $t_s = R_{So} - R_{Si}$.

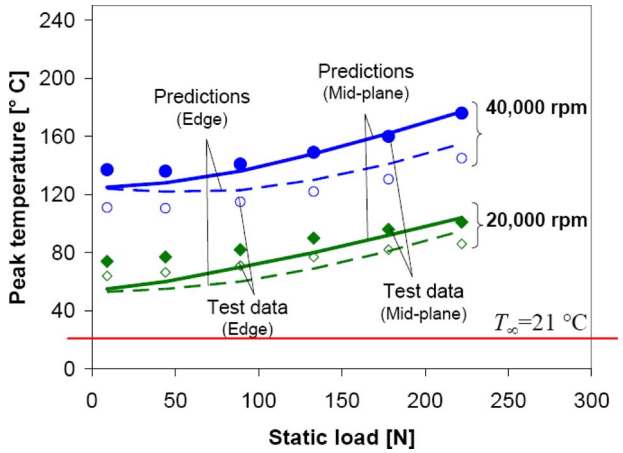

Fig. 7 Predicted film temperatures at bearing midplane and side edge versus static load W_s at $\Theta \sim 190$ deg and for two rotor speeds, 20 krpm and 40 krpm. Air supply and ambient temperature ($T_o = T_\infty$) at 274.3 K (21 °C). Comparison to test data [6].

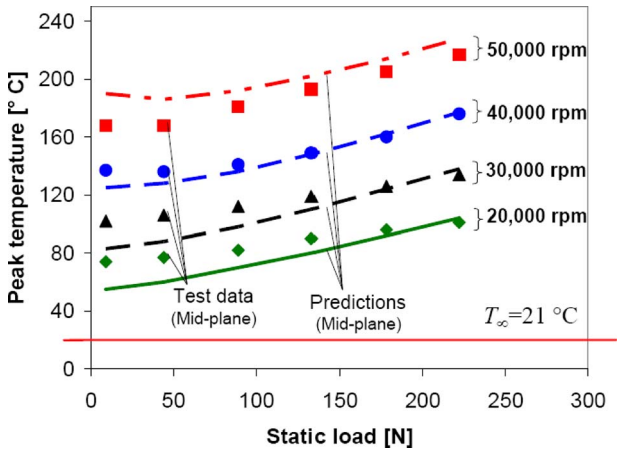

Fig. 6 Predicted film temperature at bearing midplane and $\Theta \sim 190$ deg versus static load W_s and increasing rotor speeds. Air supply and ambient temperature ($T_o = T_\infty$) at 274.3 K (21 °C). Comparison to test data [6].

$$A_1 = (R_{S_o}^2 + R_{S_i}^2)(3 + \nu_S), \quad A_2 = R_{S_i}^2(3 + \nu_S) \tag{20}$$

where E_S, ν_S, and ρ_S are the shaft material elastic modulus, Poisson ratio, and density, respectively. Figure 5 shows the predicted centrifugal growth versus rotor speed for an Inconel 718 journal (solid and hollow). The graph evidences the rapid growth of the rotor outer diameter for a thin walled shaft. Hence, journal design must consider this effect to prevent failure due to shaft (thermal) seizure, as stressed in Ref. [7].

For increasing rotor speeds, 20–50 krpm, Fig. 6 shows the predicted film temperature and test data from Ref. [6] at the bearing axial midplane and circumferential angle $\Theta \sim 190$ deg versus applied static load W_s along the vertical downwards direction. Symbols denote the test data,[5] while continuous lines represent the THD model predictions. The maximum static load $W_s = 222$ N represents a low specific pressure, $W_s/LD = 1.08$ bar (15.9 psi). As expected, the film temperature grows as the static load increases and as the rotor speed increases. Note that both predicted and measured temperatures are higher than ambient, i.e., $T_f \gg 274.3$ K (21 °C), even for operation with the bearing dead weight of just 9 N. The large temperature increase (>100 °C, even with the smallest load of 9 N at 50 krpm, for example) is representative of an inefficient cold gas supply condition; hence, the assumed thermal mixing coefficient $\lambda = 0.65$ [6] is representative of the test GFB and data. The need of a forced outer cooling gas stream is apparent. As the static load increases to 222 N, the film temperature increases mildly.

Figure 7 depicts the predicted gas film temperatures at the bearing midplane and near side edge versus static load for two rotor speeds, 20 krpm and 40 krpm. The measurements and predictions refer to circumferential angle $\Theta \sim 190$ deg. The temperature grows as the rotor speed increases and as the static load increases. In general, the difference in film temperatures at the midplane and edge (axial thermal gradient) increases as the rotor speed increases. Both measurements and predictions show that the film temperature is largest at the bearing midplane, further evidencing the lack of an external cooling axial flow path. The predicted temperatures correlate favorably with the test data. Most importantly note that the film temperature (in °C) nearly doubles as the journal speed also doubles, irrespective of the applied load.

At a static load of 133 N, ($W_s/LD = 0.65$ bar), Fig. 8 shows the predicted gas film temperature distribution along the bearing axial plane ($0 < z < L$) at angle $\Theta \sim 190$ deg for increasing rotor speeds. The film temperature achieves its maximum value at the bearing midplane, and drops slightly at the side edges ($\Theta \sim 190$ deg). On the other hand, the test data show a degree of asymmetry [6]. The predictions are in good agreement with the measured temperatures, in particular at a rotor speed of 40 krpm.

The predictive analysis provides the gas film pressure and temperature fields and static load parameters, such as drag torque, power loss, and journal eccentricity. Reference [6] does not provide information on these performance parameters. Nonetheless, the predictions in Figs. 9–13 aim to reveal the effects of thermal energy on GFB performance. Figure 9 shows the predicted GFB film pressure and temperature fields for operating at a rotor speed of 20 krpm with a static load (W_s) of 89 N (specific pressure

[5]The test values do not strictly represent film temperatures. In the experiments, the temperatures reproduced in Figs. 6–8 are recorded at the outer surface of a bump strip layer and at its junction with the top foil [6]. However, the recorded temperatures are representative of the gas film, as shown later in Fig. 11.

[6]The thermal mixing parameter λ is common in oil lubricated bearings. However, the use of this parameter in gas foil bearings is novel. Since each foil bearing is essentially a custom piece of hardware, with resulting variability even in identical units, the thermal mixing parameter is largely unknown and its estimation yet to be reported.

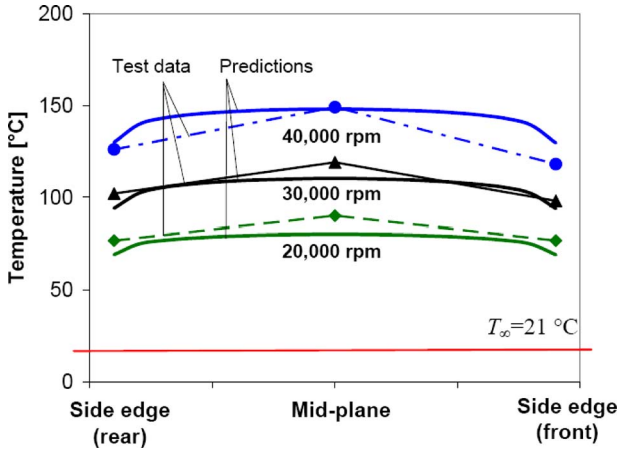

Fig. 8 Predicted axial film temperature profile for three rotor speeds and a static load W_s=133 N at Θ~190 deg. Air supply and ambient temperature (T_o=T_∞) at 274.3 K (21°C). Comparison to test data [6].

W_s/LD=0.43 bar) is typical for a generation I GFB. The predicted journal eccentricity, journal attitude angle, and minimum film thickness are 12.2 μm, 21 deg, and 9.2 μm, respectively. Along the circumferential coordinate, 0<Θ<200 deg, the film temperature increases as the gas flows and removes the shear induced mechanical energy. However, for Θ>200 deg the temperature first drops due to the reduction in hydrodynamic pressure-gas expansion that cools the gas film and further downstream, once the top foil detaches due to negligibly small shear dissipation energy. The prediction shows that the inlet gas film temperature at the top foil leading edge increases from 274.3 K (21°C) to 323.3 K (50°C), while the peak temperature of ~344.3 K (71°C) occurs at the bearing midplane, just down-

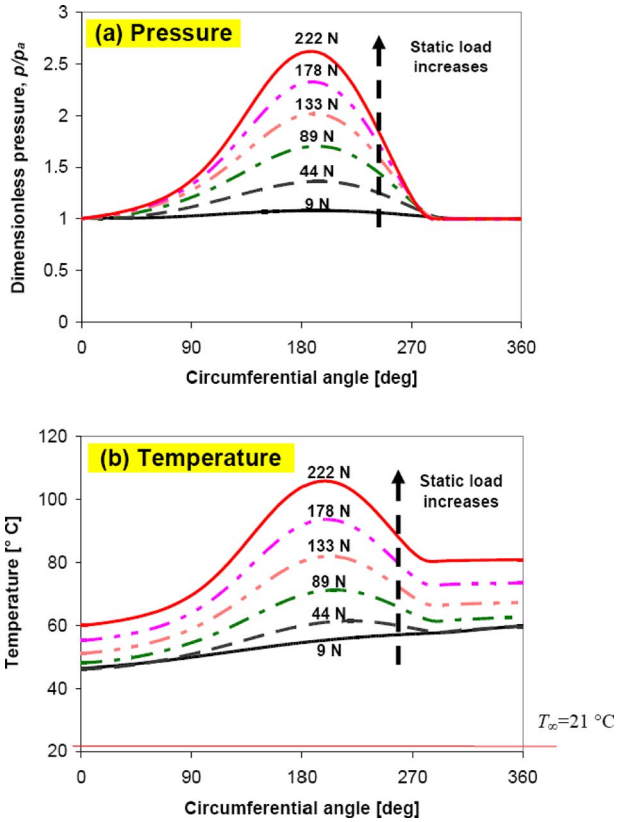

Fig. 10 Predicted film (*a*) pressure and (*b*) temperature at the bearing midplane versus angle Θ. GFB operating at 20 krpm and increasing static loads. Air supply and ambient temperature (T_o=T_∞) at 274.3 K (21°C). Thermal mixing coefficient λ =0.65.

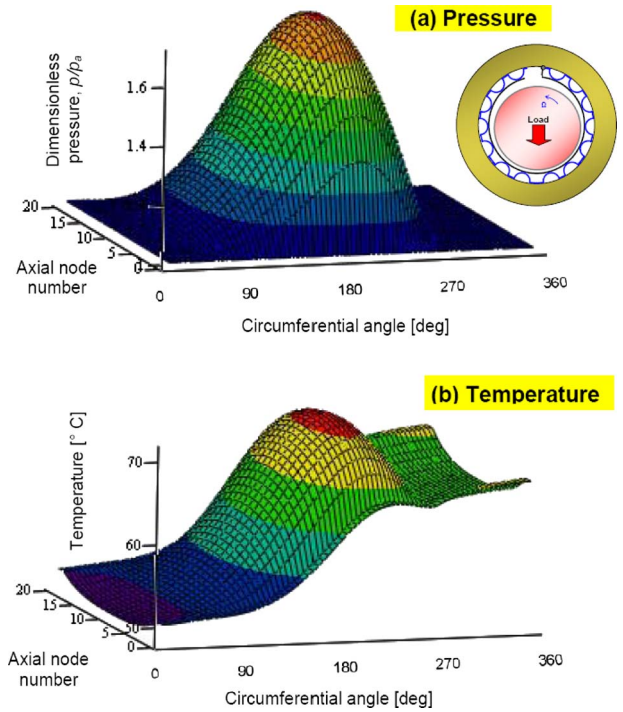

Fig. 9 Predicted film (*a*) pressure and (*b*) temperature fields in a GFB operating at a rotor speed of 20 krpm. Static load W_s =89 N. Air supply and ambient temperature (T_o=T_∞) at 274.3 K (21°C). Thermal mixing coefficient λ=0.65.

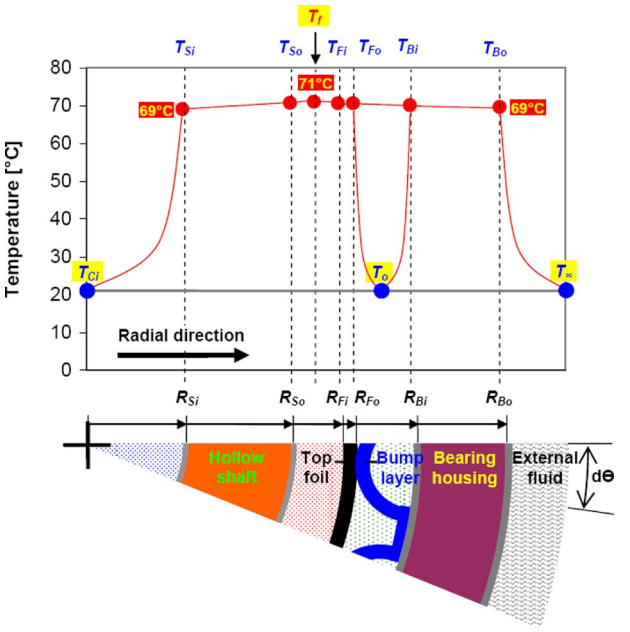

Fig. 11 Predicted radial temperature profile in GFB with rotor speed of 20 krpm and static load W_s=89 N. Peak film temperature=71°C. Air supply and ambient temperature (T_{Ci} =T_o=T_∞) at 274.3 K (21°C).

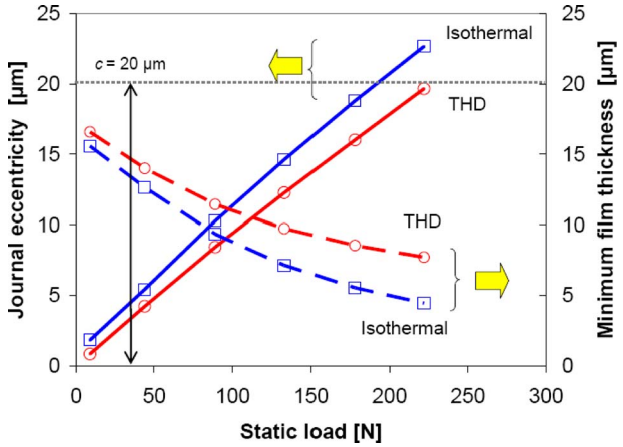

Fig. 12 Predicted journal eccentricity and minimum film thickness versus static load from isothermal and thermohydrodynamic flow models. Rotor speed=40 krpm. Air supply and ambient temperature ($T_o=T_\infty$) at 274.3 K (21°C).

stream of the peak film pressure at an angle of ~200 deg. Note that the Couette flow approximation [11,31] would predict a peak film temperature at the trailing edge of the top foil. The approximation is strictly valid for operation at small journal eccentricities and ignores the effect of fluid compressibility. The Couette flow assumption underestimates the actual peak film temperature, in particular, for heavily loaded GFBs.

Figure 10 presents the film pressure and temperature at the bearing midplane versus circumferential coordinate for increasing static loads at a rotor speed of 20 krpm. Both the peak pressure and temperature increase as the static load increases. Note the peak film temperature at the trailing edge of the top foil with the smallest load of 9 N.

For rotor operation at 20 krpm and with a static load W_s =89 N (as in Fig. 9), Fig. 11 displays the predicted radial temperature profile in the GFB. Note that the bearing OD and shaft ID are exposed to ambient temperature $\{T_g=274.3\ \text{K}(21°\text{C})\}$. The temperature varies little along the radial direction, i.e., the solids (shaft and bearing cartridge) are at similar temperatures since the heat flow paths are merely by material conduction in the absence of forced cooling flows, inner and outer. The drops in temperature to ambient condition take place by natural convection. Reference [6] does not report measured temperatures at the shaft and bearing

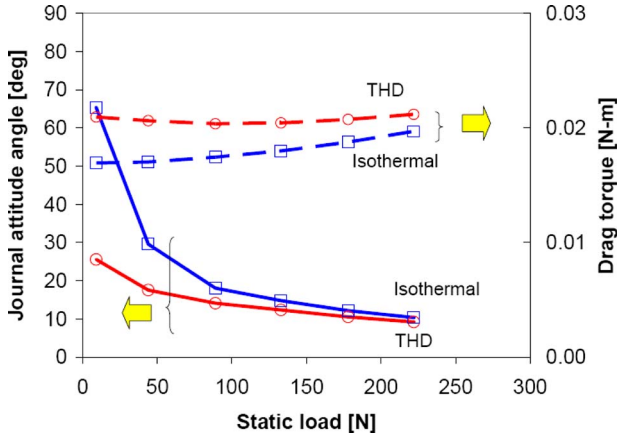

Fig. 13 Predicted journal attitude angle and drag torque versus static load for isothermal and thermohydrodynamic flow models. Rotor speed=40 krpm. Air supply and ambient temperature ($T_o=T_\infty$) at 274.3 K (21°C)

OD surfaces. However, the recorded temperatures at the back of the bump foils are assumed to represent those in the gas film, see Figs. 6–8 shown earlier.

Recently, at the authors' laboratory, temperature measurements in a hot rotor supported on GFBs show similar findings, i.e., bearing cartridge temperatures (ID and OD) a few degrees below shaft temperature [32]. The heat flow path is mainly radial.

At a rotor speed of 40 krpm, Fig. 12 displays predicted journal eccentricity and minimum film thickness versus increasing static loads. The maximum load represents $W_s/LD \sim 1$ bar (15 psi). The graph includes predictions from the current THD model and those from an isothermal flow model [22]. The isothermal model assumes a constant gas film temperature ($T_f=T_\infty$). As the static load increases, the journal eccentricity increases and the minimum film thickness decreases. The THD model predicts smaller journal eccentricities (larger minimum film thicknesses), when compared with those from the isothermal model, since an increase in the gas film temperature leads to an increase in effective gas viscosity. Note that THD predictions do account for the temperature variation in modulus of elasticity for the foil material (Inconel X750). However, this effect does not seem to affect significantly the bearing performance for moderate increases in film temperature, <473.3 K (200°C), see for example Ref. [28]. In Fig. 13, the predicted journal attitude angle decreases as the applied load increases for both THD and isothermal models. The THD model predicts a smaller journal attitude angle. Bearing drag torque first decreases and then increases from a certain load as the static load increases. A larger drag torque from the THD model is due to the increase in gas viscosity with film temperature.

4 Conclusions

Thermal management of gas foil bearings into high-temperature harsh environments demands of reliable predictive tools that account for the thermal energy transport in the gas film region, and includes the heat flux paths from the gas film into the bearing cartridge and into/from the shaft. The analysis couples the gas film pressure (Reynolds) equation to the thermal energy transport equation with appropriate boundary conditions. The model accounts for forced cooling conditions, inner and outer, and actual operating clearance determined from thermal changes in material properties and the components' thermal and centrifugal growths.

Model predictions are benchmarked against test data available in the open literature for a generation III GFB operating without forced cooling flow [6]. The reference does not provide complete information on the test bearing; hence, a number of assumptions are detailed to obtain predictions. Predictions show a peak gas film temperature at the bearing midplane and just downstream of the peak film pressure. The film peak temperature increases as the static load increases and as the rotor speed increases. As the rotor speed increases, the difference in film temperatures at the midplane and edge (axial thermal gradient) increases. Predictions are in remarkable agreement with test data. In addition, the predicted gas film temperature, as in the tests at a constant rotor speed, increases rapidly due to the absence of a forced cooling air to carry away thermal energy that is trapped due to recirculation drawn by the rotating journal, even for operation with low static loads. The THD model determines a smaller journal eccentricity (larger minimum film thickness) and larger drag torque than those obtained from an isothermal flow model, due to the increase in gas viscosity with film temperature.

Adequate thermal management of GFBs considers the changes in material properties and growth of components due to temperature and journal rotation and must integrate adequate cooling flow mechanisms that do not impose a penalty on system efficiency. Ultimately, the load capacity and reliability of the GFBs could be compromised in poorly designed and worse operated systems [5,15]. Current work at the authors' laboratory measures the thermal performance of a hot rotor supported on GFBs with an outer cooling flow [32]. Measurements of bearing and shaft tempera-

tures show the limited effectiveness of the cooling flow stream, i.e., too large flow rates are needed to reduce the bearing temperature a few degrees, in particular, for high shaft temperatures. The measurements along with THD predictions will be published in the near future.

Acknowledgment

This material is based upon work by NASA NRA on Subsonic rotary Wing, SSRW2-1.3 Oil-Free Engine Technology (Foil Gas Bearing Modeling) Grant Cooperative Agreement No. NNX07P98A. The support of the Turbomachinery Research Consortium is gratefully acknowledged. The continued interest of Dr. Samuel Howard and Dr. Christopher DellaCorte at NASA GRC is greatly appreciated.

Nomenclature

C = nominal (cold) GFB radial clearance (m)
c_+ = $c-S_C-S_T$, bearing operating radial clearance, a function of rotor speed and temperature (m)
c_p = gas specific heat at constant pressure (J/kg K)
e_X and e_Y = journal eccentricity components (m), $e=\sqrt{e_X^2+e_Y^2}$
E = Young's modulus (N/m^2)
h = film thickness (m)
$\bar{h}$ = heat convection coefficient (W/m K)
ID = inner diameter
k_B = (simple) bump-foil stiffness/unit area ($(N/m)/m^2$)
L = bearing axial width (m)
l_B = half bump arc length (m)
$\dot{m}$ = mass flow rate (kg/s)
N_b and N_s = number of bumps and number of bump strips
OD = outer diameter
P = gas pressure (Pa)
$\dot{Q}$ = heat flow per unit axial length (W/m)
$\dot{q}$ = $\dot{Q}/R$, Heat flow per unit area (W/m^2)
R = radius (m), $D=2\ R$
r = radial location (m)
Re = $\mathrm{Re}=V\ell/\upsilon$. Reynolds number, TYP velocity V and characteristic length ℓ
S_C = shaft (journal) centrifugal growth (m)
S_T = shaft (journal) thermal expansion
s_0 = bump pitch (m)
T = temperature (K)
t = time (s)
t_B = bearing cartridge thickness (m)
t_S = shaft wall thickness (m)
U and W = bulk-flow gas velocities in circumferential (x) and axial (z) directions
U_m = mean circumferential flow velocity (m/s)
W_s = static load (N)
w_d = top foil transverse deflection (m)
X and Y = inertial Cartesian coordinate system (m)
$x=R\Theta$ and z = coordinate system on plane of bearing (m)
α_T = thermal expansion coefficient (1/K)
β = gas volumetric expansion coefficient (1/K)
Δ_B = bump height (m)
Δ_{t_F} and Δ_{t_B} = top foil thickness (m), bump-foil thickness (m)
κ = thermal conductivity (W/m K)
ρ = gas density (kg/m^3)
λ = thermal inlet mixing ratio
μ = gas viscosity (Pa s)
ν = Poisson's ratio
Θ = circumferential coordinate (rad)
υ = gas kinematic viscosity, $\upsilon=\mu/\rho$ (m^2/s)
Ω = rotor angular speed (rad/s)
$\Re_g$ = ideal gas constant (J/kg K)

Subscripts

a = ambient
B, F, and S = bearing, foil, and shaft (journal)
C = cooling gas flow
eq = equivalent
f = thin gas film
i and o = inner and outer
l and t = leading and trailing edges of top foil
∞ = ambient fluid medium (stagnant)

Appendix A: Models for Heat Convection Coefficients

The Reynolds–Colburn analogy between fluid friction and heat transfer [23] for fully-developed flow determines the heat convection coefficients, accounting for heat flux from the gas film into the shaft outer surface and from the gas film into the top foil inner surface. The mean heat transfer over the entire laminar/turbulent boundary is [23,24]

$$\mathrm{St}\ \wp_r^{2/3} = f/2 \tag{A1}$$

where $\mathrm{St}=\bar{h}_{fF,fS}/\rho c_p U$ is the *Stanton* number, and ρ, c_p, and U are the fluid density, specific heat, and mean flow velocity, respectively. $\wp_r=c_p\mu/\kappa$ is the *Prandtl* number, and κ and μ are gas heat conduction coefficient and gas viscosity, respectively. f is the *Fanning* friction factor. From the relationship above, heat convection coefficients for laminar flow are derived from the Nusselt number [23,24]

$$\mathrm{Nu} = \frac{c\bar{h}_{fF,fS}}{\kappa} = 3\wp_r^{1/3} \tag{A2}$$

For effectiveness, the outer cooling flow is usually large (see Ref. [11]) to promote mixing that enhances heat transfer. Recall that the gap between the top foil back surface and the bearing inner surface is large. Hence, the outer cooling flow is likely turbulent. The heat convection coefficient is derived from Ref. [23]

$$\mathrm{Nu} = \frac{D_{\mathrm{hyd}}\bar{h}_{Fo}}{\kappa} = 0.023\ \mathrm{Re}_o^{\ 0.8}\ \wp_r^{0.4} \tag{A3}$$

where $D_{\mathrm{hyd}}=4\cdot\mathrm{area}/\mathrm{wetted\ perimeter}$ is a hydraulic diameter representing the annulus between top foil and bearing cartridge. Above $\mathrm{Re}_o=W_o D_{\mathrm{hyd}}/\upsilon_o$ is an outer flow Reynolds number with characteristic axial velocity W_o.

Without an outer cooling flow, natural heat convection coefficients to a stagnant fluidic medium are derived from [23]

$$\mathrm{Nu} = \frac{R\bar{h}}{\kappa} = 0.53(\mathrm{Gr}\cdot\wp_r)^{1/4} \tag{A4}$$

where Gr is the *Grashof* number representing thermal buoyancy effects. Equation (A4) gives heat convection coefficients $\bar{h}_{Bo}\sim\bar{h}_{B\infty}\sim\bar{h}_{Fo}\sim 6\ \mathrm{W/m^2\ K}-12\ \mathrm{W/m^2\ K}$ for surface temperatures ranging from 323.3 K to 673.3 K.

A cooling stream flowing through a hollow rotor promotes heat transfer. For a rotating cylinder with an inner axial cooling flow, Ref. [33] gives the empirical relation

$$\mathrm{Nu} = \frac{R_{S_i}\bar{h}_{Si}}{\kappa} = 0.01963\ \mathrm{Re}_{S_a}^{\ 0.9285} + 8.5101\times 10^{-6}\ \mathrm{Re}_{S_r}^{\ 1.4513}$$

$$0 < \mathrm{Re}_{S_a} = \frac{\Omega R_{S_i}(2R_{S_i})}{\upsilon_{C_i}} < 3 \times 10^4, \quad 1.6 \times 10^3 < \mathrm{Re}_{S_a}$$

$$= \frac{W_{C_i}(2R_{S_i})}{\upsilon_{C_i}} < 2.77 \times 10^5 \tag{A5}$$

where Re_{S_a} and Re_{S_r} are axial and circumferential (inner) flow Reynolds numbers.

References

[1] DellaCorte, C., and Bruckner, R. J., 2007, "Oil-Free Rotor Support Technologies for an Optimized Helicopter Propulsion System," Report No. NASA/TM2007-214845.

[2] DellaCorte, C., and Valco, M. J., 2000, "Load Capacity Estimation of Foil Air Journal Bearings for Oil-Free Turbomachinery Applications," Report No. NASA/TM2000-209782.

[3] Heshmat, H., 1994, "Advancements in the Performance of Aerodynamic Foil Journal Bearings: High Speed and Load Capacity," ASME J. Tribol., **116**, pp. 287–295.

[4] Radil, K., DellaCorte, C., and Zeszotek, M., 2007, "Thermal Management Techniques for Oil-Free Turbomachinery Systems," STLE Tribol. Trans., **50**, pp. 319–327.

[5] Radil, K., Howard, S., and Dykas, B., 2002, "The Role of Radial Clearance on the Performance of Foil Air Bearings," STLE Tribol. Trans., **45**, pp. 485–490.

[6] Radil, K. C., and Zeszotek, M., 2004, "An Experimental Investigation Into the Temperature Profile of a Compliant Foil Air Bearing," STLE Tribol. Trans., **47**(4), pp. 470–479.

[7] Dykas, B., and Howard, S. A., 2004, "Journal Design Considerations for Turbomachine Shafts Supported on Foil Air Bearings," STLE Tribol. Trans., **47**(4), pp. 508–516.

[8] Kim, T. H., Breedlove, A. W., and San Andrés, L., 2008, "Characterization of Foil Bearing Structure for Increasing Shaft Temperatures: Part I–Static Load Performance," ASME Paper No. GT2008-50567.

[9] Kim, T. H., Breedlove, A. W., and San Andrés, L., 2008, "Characterization of Foil Bearing Structure for Increasing Shaft Temperatures: Part II–Dynamic Force Performance," ASME Paper No. GT2008-50570.

[10] Lee, Y.-B., Jo, J.-H., Park, D.-J., Kim, C.-H., and Rhim, Y.-C., 2006, "Dynamic Characteristics of Bump Foils Considering With Thermal Effect in Air Foil Bearings," ASME Paper No. IJTC2006-12189.

[11] Salehi, M., Swanson, E., and Heshmat, H., 2001, "Thermal Features of Compliant Foil Bearings—Theory and Experiments," ASME J. Tribol., **123**, pp. 566–571.

[12] Peng, Z.-C., and Khonsari, M. M., 2006, "A Thermohydrodynamic Analysis of Foil Journal Bearings," ASME J. Tribol., **128**, pp. 534–540.

[13] Le Lez, S., 2007, "Caracterisques Statiques Et Dynaniques Des Paliers A Feuilles," Ph.D. thesis, Universite De Poitiers, Poitiers, France.

[14] Feng, K., and Kaneko, S., 2008, "A Study of Thermohydrodynamic Features of Multiwound Foil Bearing Using Lobatto Point Quadrature," ASME Paper No. GT2008-50110.

[15] DellaCorte, C., 1997, "A New Foil Air Bearing Test Rig for Use to 700°C and 70,000 rpm," Report No. NASA/TM1997-107405.

[16] Sim, K., and Kim, D., 2008, "Thermohydrodynamic Analysis of Compliant Flexure Pivot Tilting Pad Gas Bearings," ASME J. Eng. Gas Turbines Power, **130**(3), p. 032502.

[17] Lubell, D., DellaCorte, C. and Stanford, M., 2006, "Test Evolution and Oil-Free Engine Experience of a High Temperature Foil Air Bearing Coating," ASME Paper No. GT2006-90572.

[18] Kim, T. H., and San Andrés, L., 2009, "Effect of Side End Pressurization on the Dynamic Performance of Gas Foil Bearings: A Model Anchored to Test Data," ASME J. Eng. Gas Turbines Power, **131**(1), p. 012501.

[19] Black, H. F., Allaire, P. E., and Barrett, L. E., 1981, "Inlet Flow Swirl in Short Turbulent Annular Seal Dynamics," *Proceedings of the Ninth International Conference in Fluid Sealing*, BHRA Fluid Engineering, Leeuwenborst, The Netherlands, pp. 141–152.

[20] Childs, D., 1993, *Turbomachinery Rotordynamics–Phenomena, Modeling, & Analysis*, Wiley, New York, pp. 248–274.

[21] Kim, T. H., and San Andrés, L., 2008, "Heavily Loaded Gas Foil Bearings: A Model Anchored to Test Data," ASME J. Eng. Gas Turbines Power, **130**(1), p. 012504.

[22] San Andrés, L., and Kim, T. H., 2008, "Analysis of Gas Foil Bearings Integrating FE Top Foil Models," Tribol. Int., **42**(1), pp. 111–120.

[23] Holman, J. P., 1990, *Heat Transfer*, McGraw-Hill, New York, pp. 245–247.

[24] San Andrés, L., and Kim, T. H., 2008, "Thermohydrodynamic Analysis of Bump Type Gas Foil Bearings: Model and Predictions," Texas A&M University, College Station, TX, Technical Report No. TRC-B&C-2-08.

[25] Kim, T. H., and San Andrés, L., 2006, "Limits for High Speed Operation of Gas Foil Bearings," ASME J. Tribol., **128**, pp. 670–673.

[26] Ruscitto, D., Mc Cormick, J., and Gray, S., 1978, "Hydrodynamic Air Lubricated Compliant Surface Bearing for an Automotive Gas Turbine Engine I-Journal Bearing Performance," NASA Report No. NASA CR-135368.

[27] White, F. M., 1994, *Fluid Mechanics*, McGraw-Hill, New York.

[28] Kutz, M., 2005, *Mechanical Engineers' Handbook: Materials and Mechanical Design*, Vol. 1, Wiley, New York, Chap. 8.

[29] Iordanoff, I., 1999, "Analysis of an Aerodynamic Compliant Foil Thrust Bearing: Method for a Rapid Design," ASME J. Tribol., **121**, pp. 816–822.

[30] Timoshenko, S. P., and Goodier, J. N., 1970, *Theory of Elasticity*, McGraw-Hill, New York, pp. 80–83.

[31] Pinkus, O., and Sternlicht, B., 1961, *Theory of Hydrodynamic Lubrication*, McGraw-Hill, New York, pp. 14–22.

[32] Kim, T. H., and San Andrés, L., 2008, "Rotordynamic Measurements on a High Temperature Rotor Supported on Gas Foil Bearings," Texas A&M University, College Station, TX, Technical Report No. TRC-B&C-3-08.

[33] Seghir-Ouali, S., Saury, D., Harmand, S., Phillipart, O., and Laloy, D., 2006, "Convective Heat Transfer Inside a Rotating Cylinder With an Axial Air Flow," Int. J. Therm. Sci., **45**, pp. 1166–1178.